The Induction Motor MRAS-Based Speed Estimator Capable of Modelling the Slip Frequency Dependent Variability of the Rotor Impedance

Grzegorz Utrata [1],* and Jaroslaw Rolek [2]

[1] Faculty of Electrical Engineering, Czestochowa University of Technology, 17 Armii Krajowej Ave., 42-200 Czestochowa, Poland

[2] Faculty of Electrical Engineering, Automatic Control and Computer Science, Kielce University of Technology, 7 Tysiaclecia Panstwa Polskiego Ave., 25-314 Kielce, Poland; jrolek@tu.kielce.pl

* Correspondence: grzegorz.utrata@pcz.pl

Abstract: Speed feedback is indispensable not only for closed-loop controlled induction motors (IM) but also for the state monitoring systems of open-loop controlled IMs. Replacing speed sensors with speed estimations has many advantages including, e.g., hardware complexity reduction, sensor cabling elimination, and reduction of IM drive costs. From the various methods for IM speed estimation proposed in the literature, the model reference adaptive system (MRAS)-based speed estimator stands out because of its straightforward synthesis technique and lower computational complexity. On the other hand, this estimator is inherently sensitive to mismatching of IM equivalent circuit parameters. During transients, when the slip frequency cannot be temporarily controlled over the assumed operating point, rotor impedance varies with the slip frequency changes. This phenomenon is even more significant for open-loop controlled high-slip IMs (NEMA design D IMs), which operate under the cycling load like in, e.g., oil well pumps. The rate and the range of rotor impedance variability are related to the rate and the range of the slip frequency changes. Therefore, a speed estimator capable of modelling the slip frequency dependent variability of the rotor impedance may be required, particularly for the state monitoring systems of open-loop controlled IMs. This paper presents an MRAS-based speed estimator developed on the IM space vector model with the rotor impedance variability modelled by the parallel connected branches of the series rotor equivalent resistance and leakage inductance. The experimental test results confirm the precise speed estimation of the tested IMs achieved by the devised MRAS-based speed estimator in the considered slip frequency range and indicate its potential industrial application.

Keywords: induction motors; speed estimation; MRAS; equivalent circuit; deep-bar effect

1. Introduction

Variable frequency induction motor (IM) drives are widely employed in many industrial applications because of their wide-range speed control, overall reliability, and mechanical robustness. Speed-sensorless control or speed-sensorless state monitoring systems are attractive technologies due to their advantages over drives equipped with a speed sensor, such as reduced hardware complexity and lower cost, reduced size of the drive machine, elimination of the sensor cable, and better noise immunity [1,2]. Speed-sensorless control or speed-sensorless state monitoring systems additionally grow in importance with regard to motors operated in hostile environments. Moreover, speed estimation ensures that IM drives equipped with a speed sensor can continue to operate in the case of its failure. All of these factors contributed to the significant advancement of the state of the art in developing speed estimation methods for IM drives.

Various speed estimation methods for closed-loop controlled IMs have been proposed in the literature [1–3]. A lot of attention has been devoted to methods developed based on

IM space vector models. With these methods, the IM speed is obtained through estimators relying on the adaptive control with reference model technique [4–9], adaptive state observers [10–12], sliding-mode state observers [13,14], or from extended state observers or Kalman filters where the IM speed is considered as an additional state variable [15–20]. The model-based methods are capable of accurately tracking IM speed across a wide range, however there are some limitations to their performance in low and zero speed regions [1–3,5–9]. Additionally, these methods are inherently more or less sensitive to variability of the IM equivalent circuit parameters, in particular, the stator and rotor resistances [1,2,21–25].

In parallel to the model-based methods, much work has been invested into the development of methods utilizing motor saliency for IM speed estimation. These methods retrieve information on IM speed from rotor slot or air-gap eccentricity spectral components inherently included in stator currents or voltage source inverter supply currents [26–28]. Alternatively, the specified high-frequency carrier voltage signals are injected along with the IM supply voltages, which are modulated by the actual spatial orientations of motor saliencies. This provides the carrier frequency components in stator currents, which are subsequently extracted, demodulated, and processed to estimate the required information (i.e., the IM speed or the rotor flux angular position) [29–33]. The motor saliency-based methods enable accurate IM speed estimation across the whole speed range when the signal injection is employed. These methods are also less sensitive than model-based methods or completely insensitive to variability of the IM equivalent circuit parameters. However, the use of motor saliency-based methods is associated with some difficulties, such as the low spectral separation between the useful signal and disturbances and the low signal to noise ratio. Therefore, these methods employ computation-intensive signal processing procedures. Moreover, some of these methods require a custom-designed rotor slot opening to further enhance the motor saliencies [29].

The model reference adaptive system (MRAS) can be effectively adopted for IM speed estimation [4]. The MRAS-based speed estimator is characterised by a straightforward synthesis technique and less computational complexity in comparison to the aforementioned IM speed estimation methods. With the MRAS-based speed estimator proposed in [4], the IM speed estimate is tuned using the error signal, which is proportional to the angular displacement between the two rotor flux space vectors obtained by the different flux estimators: voltage and current models. The voltage model is sensitive to stator resistance thermal variability and the poor voltage signal to noise ratio that is measured in low and zero speed regions when the stator resistance voltage drop becomes relevant compared to the stator electromotive force. The current model performance, on the other hand, is affected by rotor time constant variability.

During transients when the slip frequency cannot be temporarily controlled over the assumed operating point, such as rapid torque disturbances or speed command changes, rotor impedance varies with the slip frequency changes. This phenomenon is even more significant for open-loop controlled high-slip IMs (NEMA design D IMs) which operate under the cycling load, such as in the case of oil well pumps. The rate and the range of rotor impedance variability are related to the rate and the range of the slip frequency changes.

Different modifications of the MRAS-based speed estimator for the closed-loop controlled IM have been proposed in the literature, with the main attention being placed on eliminating the drawbacks of the rotor flux voltage model, which lead to instability problems in low and zero speed regions [5–9]. The impact of rotor impedance variability on the performance of the MRAS-based speed estimator has attracted considerably less attention [21,34,35], but is still the subject of studies and can be developed for use in, e.g., the speed-sensorless state monitoring systems for open-loop controlled IMs.

This paper presents a novel MRAS-based speed estimator that is capable of modelling how slip frequency changes affect rotor impedance variability. The proposed speed estimator was devised using the IM space vector model with the rotor impedance variability being modelled by the parallel connected branches of the series rotor equivalent resistance and leakage inductance. As a result, such an estimator enables speed estimations in an

arbitrarily wide slip frequency range which is determined by the IM space vector model so that the wider range of slip frequencies is of interest and the greater order of the rotor equivalent circuit is required for accurate rotor impedance variability approximation. Thus, the speed estimation is not restricted to the range around the rated slip frequency like it is in the model-based methods presented in the literature so far. Therefore, this estimator can be especially useful in the speed-sensorless state monitoring system for open-loop controlled IMs, particularly the high-slip motors.

The synthesis technique for the novel MRAS-based speed estimator was carried out simply by adopting the technique described in [4]. The investigations presented in the paper are mainly focused on verifying the performance of the MRAS-based speed estimator under the rotor impedance variability that occurs with slip frequency changes. The performance of the proposed MRAS-based speed estimator was verified experimentally on the squirrel-cage rotor (CR) and solid rotor (SR) IMs that have torque-speed characteristics corresponding to the ANSI/NEMA MG 1-2021 design B and D IMs, respectively.

2. Rotor Flux Mathematical Models

The dynamic analysis and control of IMs are generally performed on their space vector mathematical models. The literature presents IM space vector models where the rotor impedance variability results from the skin effect that occurs in rotor bars (also called the rotor deep-bar effect) and is modelled by different configurations of connections for rotor equivalent resistances and leakage inductances, expressed typically in the I-, T-, Π- or mirror Γ-networks, which are connected in cascade [36–39]. The choice of the two-terminal-pair network type is a compromise between the possible modelling accuracy of the rotor impedance variability and the computational complexity of the IM space vector model [36]. The number N of the cascade-connected, two-terminal-pair networks is related to the studied range of slip frequencies ω_2 in such a way that the wider range of slip frequencies is considered and a greater order of the rotor equivalent circuit is required for close modelling of the rotor impedance variability.

The reasonable choice for an IM space vector model for designing the rotor flux estimator intended for field-oriented control or speed estimation is the one with the least computational complexity possible. The works [37,38] present studies on the IM space vector model where the rotor impedance variability related to the skin effect was modelled by the parallel connected branches consisting of the series rotor equivalent resistance and leakage inductance. This mathematical model is less computationally complex compared to the models with the T-, Π-, or mirror Γ-networks since it does not involve voltage drops and currents of series impedances occurring between parallel admittances in the rotor equivalent circuit. Nonetheless, it is capable of precisely approximating the rotor impedance variability in the studied range of slip frequencies [37,38]. The stator, rotor, and flux equations of this type of IM space vector model are expressed below by (1)–(5) in the stator coordinate system (indicated by subscript "s") and the corresponding equivalent circuit is presented in Figure 1.

$$\underline{U}_{1s} = R_1 \underline{I}_{1s} + \frac{d}{dt}\underline{\Psi}_{1s} \tag{1}$$

$$0 = R_{2(n)}\underline{I}_{2(n)s} + \frac{d}{dt}\underline{\Psi}_{2(n)s} - j\omega_m\underline{\Psi}_{2(n)s} \tag{2}$$

$$\underline{\Psi}_{1s} = L_1\underline{I}_{1s} + L_m\underline{I}_{2s} \tag{3}$$

$$\underline{\Psi}_{2(n)s} = L_m(\underline{I}_{1s} + \underline{I}_{2s}) + L_{\sigma2(n)}\underline{I}_{2(n)s} \tag{4}$$

$$\underline{I}_{2s} = \sum_{n=1}^{N} \underline{I}_{2(n)s} \tag{5}$$

where: $n = 1, 2, \dots, N$, $\underline{U}_{1s}$, $\underline{I}_{1s}$, $\underline{\Psi}_{1s}$ are the stator voltage, current, and flux, respectively; $\underline{I}_{2(n)s}$ and $\underline{\Psi}_{2(n)s}$, represent the rotor current and flux, respectively, related to the nth branch

in the rotor equivalent circuit; $\underline{I}_{2s}$ is the rotor current; R_1 and L_1 stand for the stator resistance and inductance, respectively; $L_1 = L_{\sigma 1} + L_m$, $L_{\sigma 1}$ represents the stator leakage inductance; L_m is the magnetizing inductance; $R_{2(n)}$ and $L_{\sigma 2(n)}$ denote the rotor resistance and leakage inductance, respectively, related to the nth branch in the rotor equivalent circuit; and ω_m represents the electrical angular speed of the rotor, $j^2 = -1$.
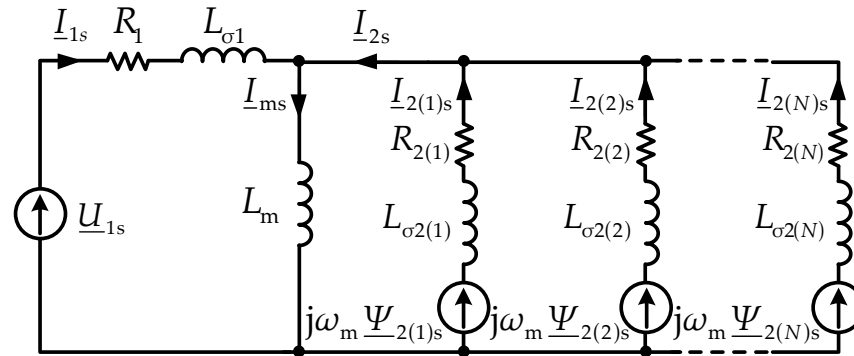
Figure 1. The IM equivalent circuit with the rotor represented by the parallel connected branches consisting of the series rotor equivalent resistance and leakage inductance.

Numerous works have been devoted to the development of IM space vector models that include the rotor deep-bar effect, but, to the best of our knowledge, the application of these types of models in an IM speed estimation scheme has not been the subject of any studies so far. Only a few works have considered the use of such models in field-oriented control algorithms [37,40], and these studies were the first to propose the airgap-flux and pseudorotor-flux oriented controlled IMs, respectively. Up to now, ref. [41] was the only study to present data regarding a rotor flux estimation scheme based on an IM space vector model including the rotor deep-bar effect. The work [41] proposed the rotor flux voltage–current model (6)–(8), which was elaborated on the IM space vector model described above (1)–(5), presented below

$$\underline{\Psi}_{2s}^{e(ui)} = L_{\sigma 2T} \sum_{n=1}^{N} \frac{\underline{\Psi}_{2(n)s}^{e}}{L_{\sigma 2(n)}} \tag{6}$$

$$T_{2(n)} \frac{\mathrm{d}}{\mathrm{d}t} \underline{\Psi}_{2(n)s}^{e} = L_m \underline{I}_{ms}^{e} - \underline{\Psi}_{2(n)s}^{e} + jT_{2(n)} \omega_m \underline{\Psi}_{2(n)s}^{e} \tag{7}$$

$$\underline{I}_{ms}^{e} = \frac{1}{L_m} \left(\int_0^t (\underline{U}_{1s} - R_1 \underline{I}_{1s}) \, \mathrm{d}t - L_{\sigma 1} \underline{I}_{1s} \right) \tag{8}$$

$$\frac{1}{L_{\sigma 2T}} = \sum_{n=1}^{N} \frac{1}{L_{\sigma 2(n)}} \tag{9}$$

$$T_{2(n)} = \frac{L_{\sigma 2(n)}}{R_{2(n)}} \tag{10}$$

where: $L_{\sigma 2T}$ stands for the total rotor leakage inductance, $T_{2(n)}$ represents the time constant of the nth branch in the rotor equivalent circuit, $\underline{I}_{ms}$ is the magnetizing current, and the superscript "e" denotes estimated variables.

The rotor flux voltage model can be described by the following equation

$$\underline{\Psi}_{2s}^{e(u)} = \frac{L_2}{L_m} \left(\int_0^t (\underline{U}_{1s} - R_1 \underline{I}_{1s}) \, \mathrm{d}t - \sigma L_1 \underline{I}_{1s} \right) \tag{11}$$

$$\sigma = 1 - \frac{L_m^2}{L_1 L_2} \tag{12}$$

where: L_2 is the rotor inductance and $L_2 = L_m + L_{\sigma 2T}$, σ represents the inductive leakage factor.

When the rotor impedance is modelled by the single branch of the series rotor equivalent resistance and leakage inductance ($N = 1$) in the IM space vector model, the rotor flux voltage–current model (6)–(8) and voltage model (11) remain valid and correspond to the commonly used IM T-type equivalent circuit. The rotor flux current model is then described by the following formula

$$T_2 \frac{\mathrm{d}}{\mathrm{d}t} \underline{\Psi}_{2s}^{e(i)} = L_m \underline{I}_{1s} - \underline{\Psi}_{2s}^{e(i)} + \mathrm{j} T_2 \omega_m \underline{\Psi}_{2s}^{e(i)} \tag{13}$$

$$T_2 = \frac{L_{\sigma 2}}{R_2} \tag{14}$$

where: R_2 and $L_{\sigma 2}$ denote the rotor resistance and leakage inductance of the IM T-type equivalent circuit, respectively.

3. MRAS-Based Speed Estimator

The MRAS-based speed estimator presented in [4] was devised on an IM space vector model with the rotor impedance represented by the single branch of the series rotor equivalent resistance and leakage inductance. It consists of the rotor flux voltage and current models operating autonomously with each other. The rotor flux voltage model (11) serves as the reference since it does not involve the IM speed. In contrast, the current model (13) incorporates the IM speed and therefore plays the role of the adjustable model. The rotor flux estimates are then fed into the input of the properly designed adaptation mechanism that generates the IM speed estimate for the adjustable model. The IM MRAS-based speed estimator described in [4] will be referred to as the MRAS$^{(u-i)}$ throughout this paper.

The adjustable mechanism in [4] was designed by relying on the synthesis technique for the MRAS structures, which is based on the concept of hyperstability [42]. This approach assures that the MRAS state error equation is globally asymptotically stable.

The equality of the rotor flux estimates generated by both of the MRAS$^{(u-i)}$ models can be achieved when the actual IM speed is used to drive the adjustable model (15). Then, the state error equation between the rotor flux estimates obtained through the voltage model and the current model driven by the IM speed estimate generated by the adaptation mechanism can be expressed by (16)–(18)

$$\underline{\Psi}_{2s}^{e(u)} = \underline{\Psi}_{2s}^{e(i)}(\omega_m) \tag{15}$$

$$\frac{\mathrm{d}}{\mathrm{d}t} \begin{bmatrix} \varepsilon_\alpha \\ \varepsilon_\beta \end{bmatrix} = \begin{bmatrix} -\frac{1}{T_2} & -\omega_m \\ \omega_m & -\frac{1}{T_2} \end{bmatrix} \begin{bmatrix} \varepsilon_\alpha \\ \varepsilon_\beta \end{bmatrix} + \begin{bmatrix} -\Psi_{2\beta}^{e(i)}(\omega_m^e) \\ \Psi_{2\alpha}^{e(i)}(\omega_m^e) \end{bmatrix} (\omega_m - \omega_m^e) \tag{16}$$

$$\varepsilon_\alpha = \Psi_{2\alpha}^{e(u)} - \Psi_{2\alpha}^{e(i)}(\omega_m^e) \tag{17}$$

$$\varepsilon_\beta = \Psi_{2\beta}^{e(u)} - \Psi_{2\beta}^{e(i)}(\omega_m^e) \tag{18}$$

where: $\Psi_{2\alpha}$ and $\Psi_{2\beta}$ are the α and β components of the rotor flux space vector in the stator coordinate system, respectively, and ε_α and ε_β represent the errors between the rotor flux components estimated by the reference and the adjustable models of the MRAS$^{(u-i)}$. The following notations for the rotor flux estimates $\underline{\Psi}_{2s}^e(\omega_m)$ and $\underline{\Psi}_{2s}^e(\omega_m^e)$ are used only for the state error equations to distinguish whether the actual or estimated IM speed was employed in the rotor flux model.

The adaptation mechanism adopted in [4] is expressed by the following equation:

$$\omega_m^e = \Phi_2(\varepsilon_\alpha, \varepsilon_\beta) + \int_0^t \Phi_1(\varepsilon_\alpha, \varepsilon_\beta)\, \mathrm{d}t \tag{19}$$

The functions $\Phi_1(\varepsilon_\alpha, \varepsilon_\beta)$ and $\Phi_2(\varepsilon_\alpha, \varepsilon_\beta)$ were determined by solving Popov's inequality (20) and took the forms described by Equations (21) and (22) [4]. Consequently, the IM speed estimate can be tuned through the proportional plus integral controller driven by the error signal proportional to the angular displacement between the rotor flux estimates which are generated by the reference and adjustable models of the MRAS$^{(u-i)}$. The MRAS$^{(u-i)}$ schematic diagram is presented in Figure 2.

$$\int_0^{t_1} \left[\left(\varepsilon_\alpha \Psi_{2\beta}^{e(i)} - \varepsilon_\beta \Psi_{2\alpha}^{e(i)} \right) \left(\omega_m - \omega_m^e \right) \right] dt \geq -\gamma_0^2 \tag{20}$$

$$\Phi_1\left(\varepsilon_\alpha, \varepsilon_\beta\right) = K_2 \left(\varepsilon_\beta \Psi_{2\alpha}^{e(i)} - \varepsilon_\alpha \Psi_{2\beta}^{e(i)} \right) \tag{21}$$

$$\Phi_2\left(\varepsilon_\alpha, \varepsilon_\beta\right) = K_1 \left(\varepsilon_\beta \Psi_{2\alpha}^{e(i)} - \varepsilon_\alpha \Psi_{2\beta}^{e(i)} \right) \tag{22}$$

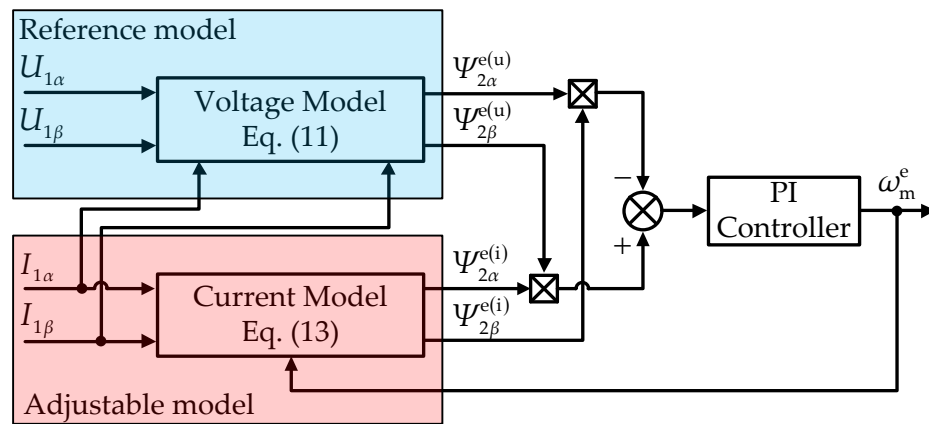where γ_0 is a positive constant and K_1 and K_2 stand for the adaptation mechanism gain constants.

Figure 2. The schematic diagram of the MRAS$^{(u-i)}$.

Since the rotor flux current model (13) involves the rotor time constant, the rotor flux estimate is inherently affected by the mismatch between the rotor equivalent circuit parameters and the actual rotor impedance. Therefore, to maintain the high precision of the IM MRAS-based speed estimator during transients or cycling load changes, its reference and adjustable models should be either insensitive to the rotor impedance variability that occurs with the slip frequency changes or capable of accurately modelling this variability. Thus, a promising candidate for the MRAS adjustable model is the rotor flux voltage–current model (6)–(8) formulated on the IM space vector model where the rotor impedance variability is modelled by the N parallel connected branches of the series rotor equivalent resistance and leakage inductance. In this case, the rotor flux voltage model (11) can be used as the MRAS reference model since it does not involve the rotor resistance and so its sensitivity to the rotor impedance variability related to the skin effect in rotor bars is basically limited. This configuration of the MRAS-based speed estimator will be marked as the MRAS$^{(u-ui)}$ throughout the paper.

The equality of the rotor flux estimates generated by the voltage model (11) and the voltage–current model (6)–(8) driven by the actual IM speed can be expressed as follows:

$$\underline{\Psi}_{2s}^{e(u)} = \underline{\Psi}_{2s}^{e(ui)}(\omega_m) = L_{\sigma 2T} \sum_{n=1}^{N} \frac{\underline{\Psi}_{2(n)s}^{e(ui)}(\omega_m)}{L_{\sigma 2(n)}} \tag{23}$$

Then, the state error equation between the estimates of these rotor flux models, where the IM speed estimate drives the voltage–current model, can be expressed in the analogous form as shown in (16):

$$\frac{\mathrm{d}}{\mathrm{d}t}\begin{bmatrix}\varepsilon'_\alpha \\ \varepsilon'_\beta\end{bmatrix} = L_{\sigma 2\mathrm{T}}\sum_{n=1}^{N}\frac{1}{L_{\sigma 2(n)}}\begin{bmatrix}-\frac{1}{T_{2(n)}} & -\omega_\mathrm{m} \\ \omega_\mathrm{m} & -\frac{1}{T_{2(n)}}\end{bmatrix}\begin{bmatrix}\varepsilon'_{(n)\alpha} \\ \varepsilon'_{(n)\beta}\end{bmatrix} +$$
$$+ L_{\sigma 2\mathrm{T}}\sum_{n=1}^{N}\frac{1}{L_{\sigma 2(n)}}\begin{bmatrix}-\Psi^{\mathrm{e(ui)}}_{2(n)\beta}(\omega^\mathrm{e}_\mathrm{m}) \\ \Psi^{\mathrm{e(ui)}}_{2(n)\alpha}(\omega^\mathrm{e}_\mathrm{m})\end{bmatrix}(\omega_\mathrm{m}-\omega^\mathrm{e}_\mathrm{m}) \tag{24}$$

$$\varepsilon'_\alpha = \Psi^{\mathrm{e(u)}}_{2\alpha} - \Psi^{\mathrm{e(ui)}}_{2\alpha}(\omega^\mathrm{e}_\mathrm{m}) \tag{25}$$

$$\varepsilon'_\beta = \Psi^{\mathrm{e(u)}}_{2\beta} - \Psi^{\mathrm{e(ui)}}_{2\beta}(\omega^\mathrm{e}_\mathrm{m}) \tag{26}$$

$$\varepsilon'_{(n)\alpha} = \Psi^{\mathrm{e(ui)}}_{2(n)\alpha}(\omega_\mathrm{m}) - \Psi^{\mathrm{e(ui)}}_{2(n)\alpha}(\omega^\mathrm{e}_\mathrm{m}) \tag{27}$$

$$\varepsilon'_{(n)\beta} = \Psi^{\mathrm{e(ui)}}_{2(n)\beta}(\omega_\mathrm{m}) - \Psi^{\mathrm{e(ui)}}_{2(n)\beta}(\omega^\mathrm{e}_\mathrm{m}) \tag{28}$$

Therefore, the adaptation mechanism designed for the MRAS[(u-i)] in [4] can be adopted to the MRAS[(u-ui)]. Then, the adaptation mechanism functions take the following forms:

$$\Phi'_1\big(\varepsilon'_\alpha,\varepsilon'_\beta\big) = K_2\Big(\varepsilon'_\beta\Psi^{\mathrm{e(ui)}}_{2\alpha} - \varepsilon'_\alpha\Psi^{\mathrm{e(ui)}}_{2\beta}\Big) \tag{29}$$

$$\Phi'_2\big(\varepsilon'_\alpha,\varepsilon'_\beta\big) = K_1\Big(\varepsilon'_\beta\Psi^{\mathrm{e(ui)}}_{2\alpha} - \varepsilon'_\alpha\Psi^{\mathrm{e(ui)}}_{2\beta}\Big). \tag{30}$$

The prime symbol is added to the adaptation mechanism functions and the state error Equations (24)–(30) in order to distinguish them from the ones developed in [4]. The schematic diagram of the MRAS[(u-ui)] is presented in Figure 3.
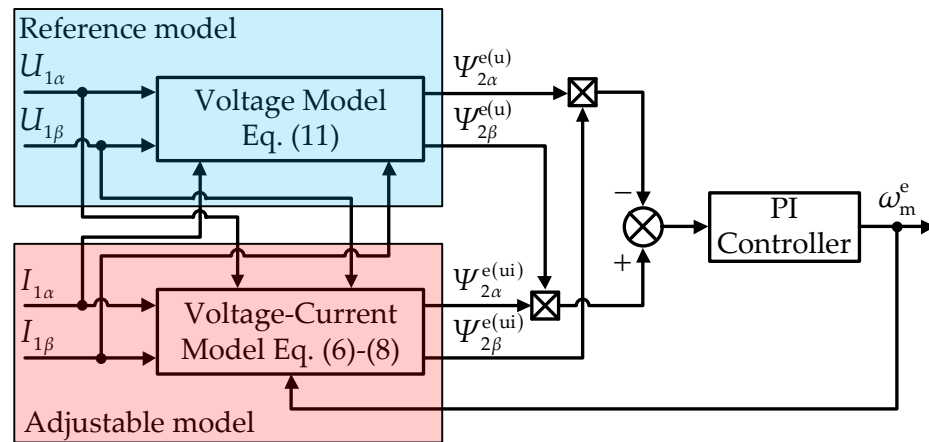

Figure 3. The schematic diagram of the MRAS[(u-ui)].

4. Experimental Results

The performance of the devised MRAS[(u-ui)] was verified experimentally on the CR and SR IMs, the rated parameters of which are listed in Appendix A (Table A1). The description, schematic diagram, and picture (Figure A2) of the laboratory test bench are included in Appendix B. The first stage of the studies was devoted to identifying the equivalent circuit parameters for the tested IMs. During this stage, the stator root-mean-square voltages and currents and stator active power, winding temperature, and rotor speed were measured under the no-load, locked rotor and load curve tests carried out according to the standard procedures [43,44]. Then the verification studies of the MRAS[(u-ui)] performance were conducted. At this stage, the instantaneous stator voltages and currents and stator winding temperature and rotor speed were measured under the specified load condition of the tested IMs.

4.1. Identification of the Equivalent Circuit Parameters

The equivalent circuit parameters of the tested CR and SR IMs are presented in Appendix A (Tables A2 and A3). The parameter sets denoted by Set B1 and Set D1 for the T-type equivalent circuit of the CR and SR IMs, respectively, were identified according to the procedure described in [43] and were based on the no-load and load curve tests. Other sets of the T-type equivalent circuit parameters were additionally employed in the verification studies to further improve their reliability. These parameters were identified using Method 4 described in [44], relying on the no-load, locked rotor, and rated load tests, and are denoted by Set B2 and Set D2.

The data gathered under the load curve tests served to determine the inductance frequency characteristics of the tested IMs. These characteristics were then used as the reference characteristics in the identification process of the IM equivalent circuit parameters where the rotor impedance is modelled by more than one ($N > 1$) parallel connected branch of the series rotor equivalent resistance and leakage inductance. The identification process was conducted in line with the procedure presented in [38]. The adopted criterion assumed the approximation of the reference characteristic modulus with an error not exceeding 2% and 5% for the CR and SR IMs, respectively, in the considered range of slip frequencies. This range corresponded to the load current adjustment range from the no-load current to around 1.75 of the IM rated current. The criterion also imposed a possible minimum approximation error of the reference characteristic argument and a minimum number N of parallel connected branches in the rotor equivalent circuit. The approximation of the reference characteristics satisfying the adopted criterion was achieved by the IM space vector model with two ($N = 2$) parallel connected branches in the rotor equivalent circuit for both tested IMs. The parameters of these models are marked by Set B3 and Set D3 for the CR and SR IMs, respectively (Tables A2 and A3).

Figures 4 and 5 present the inductance frequency characteristics of the CR and SR IMs, respectively, where the approximative characteristics determined on the IM space vector models with one and two parallel connected branches in the rotor equivalent circuit are included as well. These figures also present the modulus relative errors and the argument absolute errors between the reference and approximative characteristics.
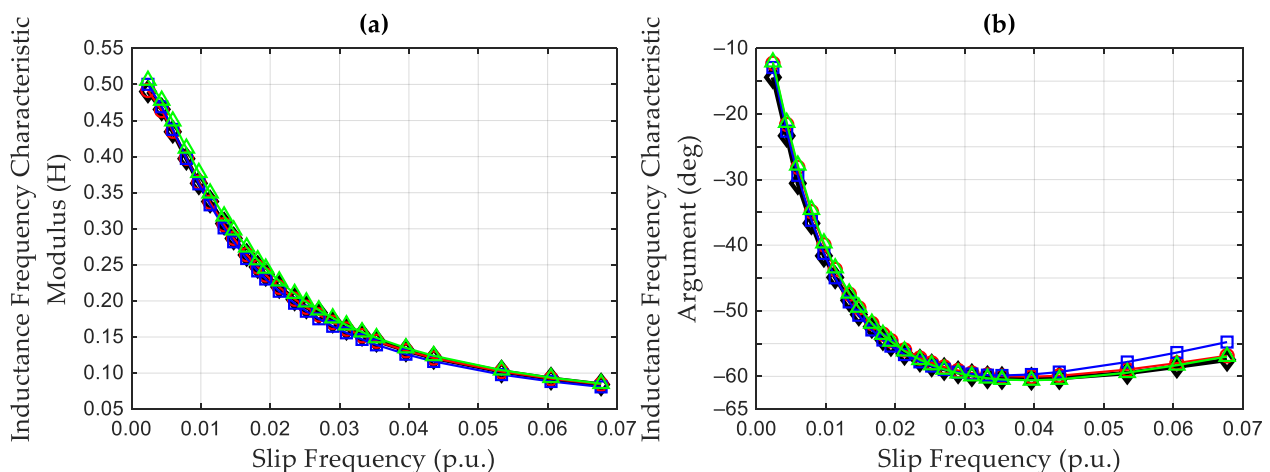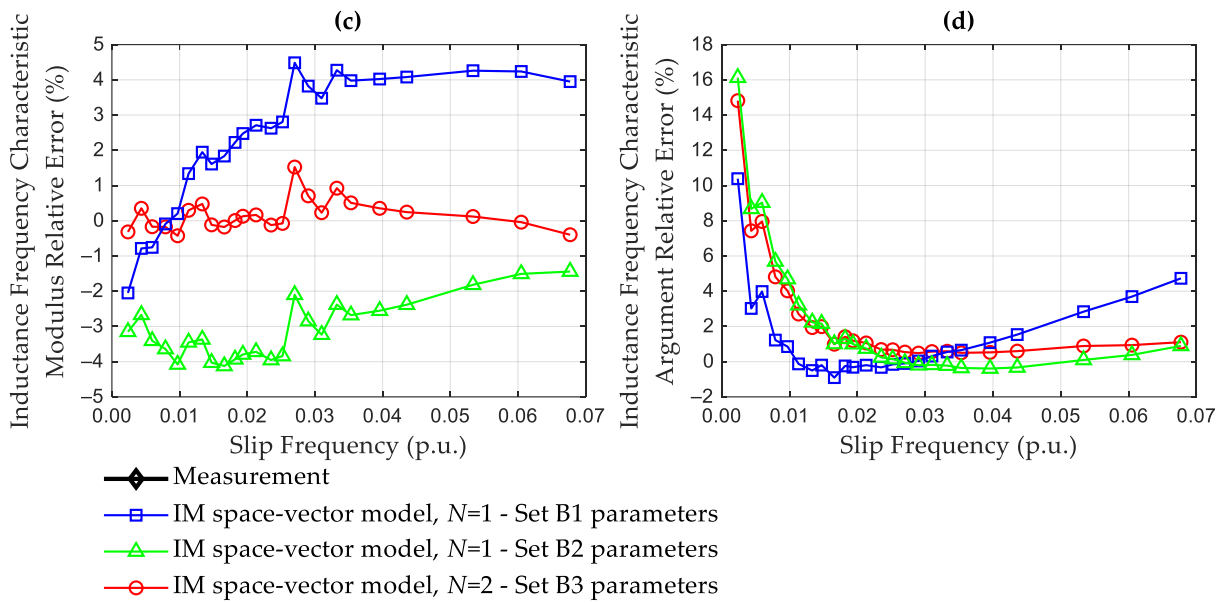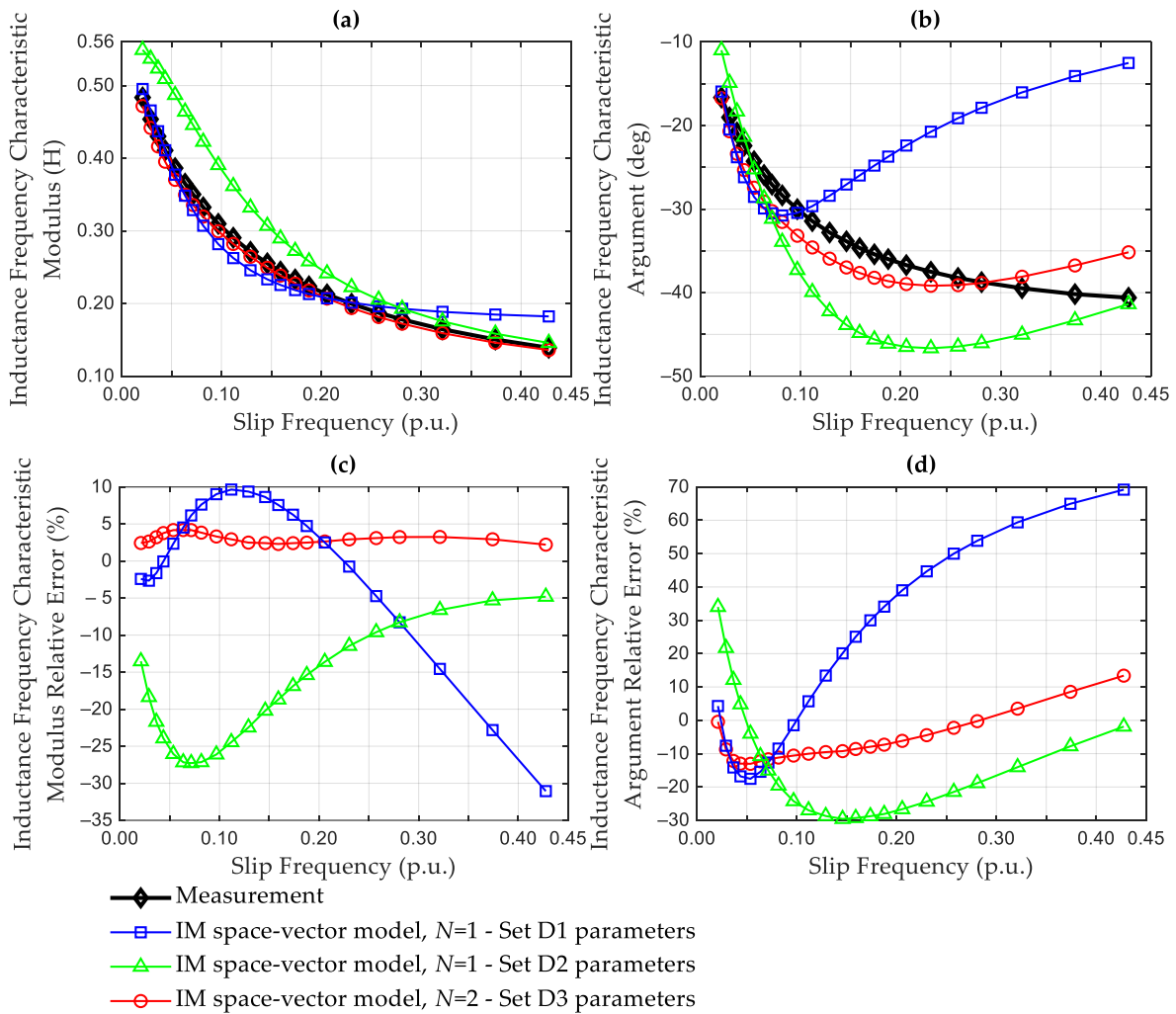

Figure 4. *Cont.*

Figure 4. The CR IM inductance frequency characteristic and its approximation by the space vector models: (**a**) modulus; (**b**) argument; (**c**) modulus relative errors; and (**d**) argument relative errors.

Figure 5. The SR IM inductance frequency characteristic and its approximation by the space vector models: (**a**) modulus; (**b**) argument; (**c**) modulus relative errors; and (**d**) argument relative errors.

The data obtained from the load curve tests additionally serve to determine the current slip characteristics of the tested IMs which are presented in Figure A1 (Appendix A). These characteristics indicate the slip frequency ranges considered under the parameter identification process for the space vector models including the rotor deep-bar effect and under the verification tests of the MRAS-based speed estimators' performance.

4.2. Verification of the Performance of the MRAS$^{(u-ui)}$

The conducted studies were mainly focused on verifying the performance of the devised MRAS$^{(u-ui)}$ under the rotor impedance variability that occurs with slip frequency changes. For this reason, the experimental tests were carried out in an open-loop drive system without speed feedback. Using this system, the slip frequency changes were forced by the load torque step command and resulted in load current changes up to 1.50 times that of the IM rated current. These tests were conducted at several IM supply frequencies, but only the results at the nominal supply frequency are included in the paper since the comparable speed estimation precision was obtained by considering estimators at all of the selected supply frequencies.

The speed estimation precision obtained by the devised MRAS$^{(u-ui)}$ underwent evaluation. Two configurations of this estimator were considered: formulated on the IM space vector models with the rotor impedance modelled by one ($N = 1$) or more than one ($N > 1$) parallel connected branches of the series rotor equivalent resistance and leakage inductance. The speed estimation precision achieved by the MRAS$^{(u-i)}$ developed in [4] served as the reference. The evaluation was carried out based on the relative errors between the measured and estimated speeds (31). To better assess the tested MRAS-speed estimators' performance, the maximal and mean relative errors of the speed estimation were additionally determined according to Equations (32) and (33), respectively,

$$\Delta\omega_{\mathrm{m}}^{\mathrm{e}} = \frac{\omega_{\mathrm{m}} - \omega_{\mathrm{m}}^{\mathrm{e}}}{\omega_{\mathrm{m}}} \, 100 \, \% \tag{31}$$

$$\max|\Delta\omega_{\mathrm{m}}^{\mathrm{e}}| = \max\left|\frac{\omega_{\mathrm{m}} - \omega_{\mathrm{m}}^{\mathrm{e}}}{\omega_{\mathrm{m}}} \, 100 \, \%\right| \tag{32}$$

$$\mathrm{M}|\Delta\omega_{\mathrm{m}}^{\mathrm{e}}| = \frac{1}{n}\sum_{i=1}^{n}\left|\frac{\omega_{\mathrm{m},i} - \omega_{\mathrm{m},i}^{\mathrm{e}}}{\omega_{\mathrm{m},i}} \, 100 \, \%\right| \tag{33}$$

where: $\omega_{\mathrm{m},i}$ and $\omega_{\mathrm{m},i}^{\mathrm{e}}$ are the ith samples of the measured and estimated speeds, respectively, and n is the number of samples.

The proportional K_1 and integral K_2 gains for the PI controllers of the considered MRAS-based speed estimators were adjusted experimentally by satisfying the compromise between the stable speed estimation, the possible low amplification of noise in speed estimates, and the possible fast rate of convergence between the components of the adaptation mechanism functions, i.e., $\underline{\Psi}_{2\alpha}^{e(u)}\underline{\Psi}_{2\beta}^{e(i)}$ and $\underline{\Psi}_{2\beta}^{e(u)}\underline{\Psi}_{2\alpha}^{e(i)}$ for the MRAS$^{(u-i)}$ and $\underline{\Psi}_{2\alpha}^{e(u)}\underline{\Psi}_{2\beta}^{e(ui)}$ and $\underline{\Psi}_{2\beta}^{e(u)}\underline{\Psi}_{2\alpha}^{e(ui)}$ for the MRAS$^{(u-ui)}$. The required rate of convergence of the adaption mechanism functions' components was achieved for proportional K_1 and integral K_2 gains equal to or greater than 2 and 10, respectively, for both tested IMs; further increasing the integral gain K_2 led to the reduction of speed estimation errors. Increasing the proportional gain above 2 had no significant effect on the speed estimation precision when the integral gain was sufficiently high. Use of a low proportional gain limited the amplification of noise in speed estimates. Figures A3 and A4 (Appendix C) present the components of the adaptation mechanism functions returned by the MRAS$^{(u-i)}$ and MRAS$^{(u-ui)}$, with the speed estimates shown in Figures 6 and 7, respectively. The fast rate of convergence between these components confirms that the PI controller gains were properly adjusted.
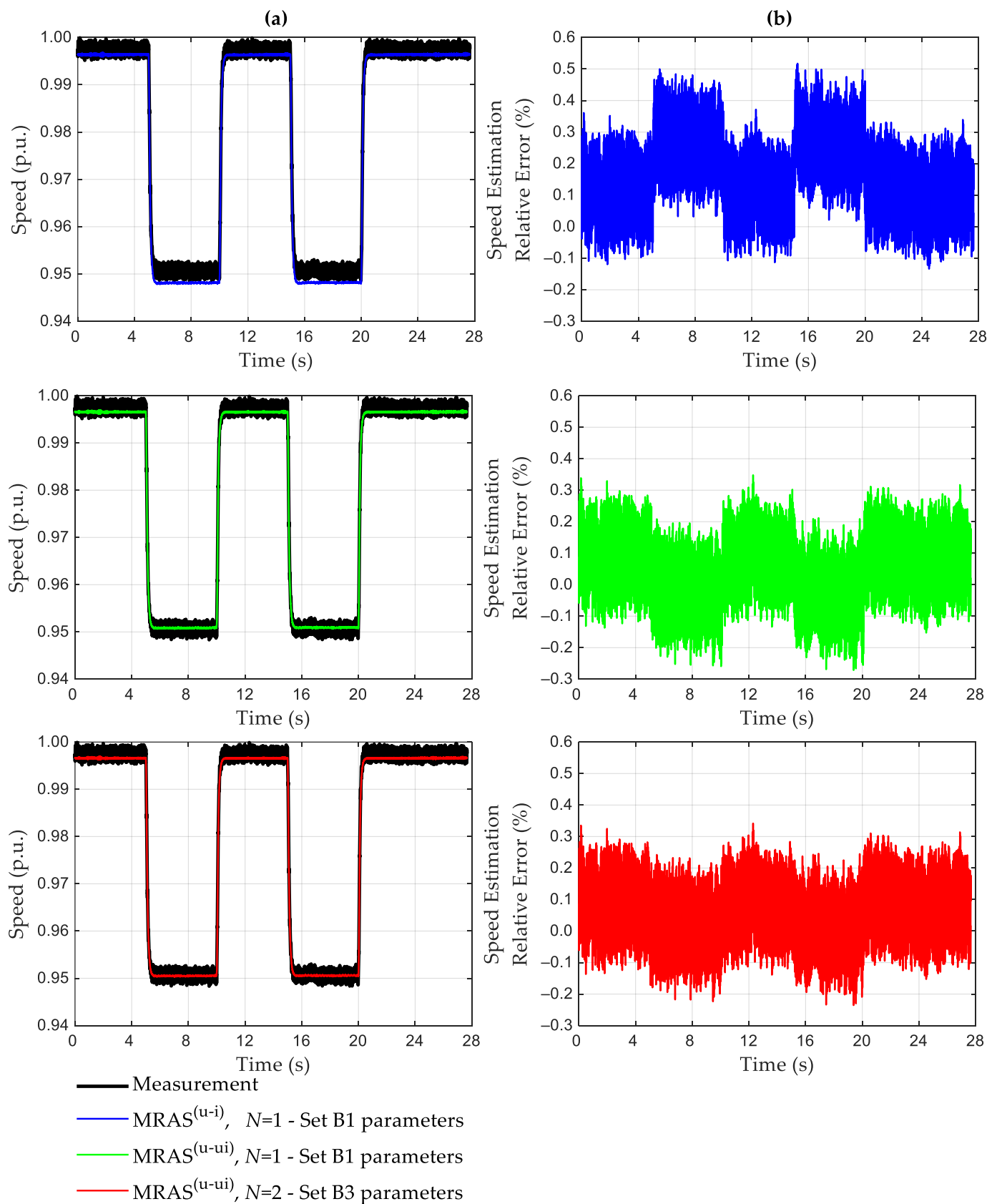
Figure 6. The speed estimation of the tested CR IM: (**a**) the measured and estimated speeds; (**b**) the speed estimation relative errors.
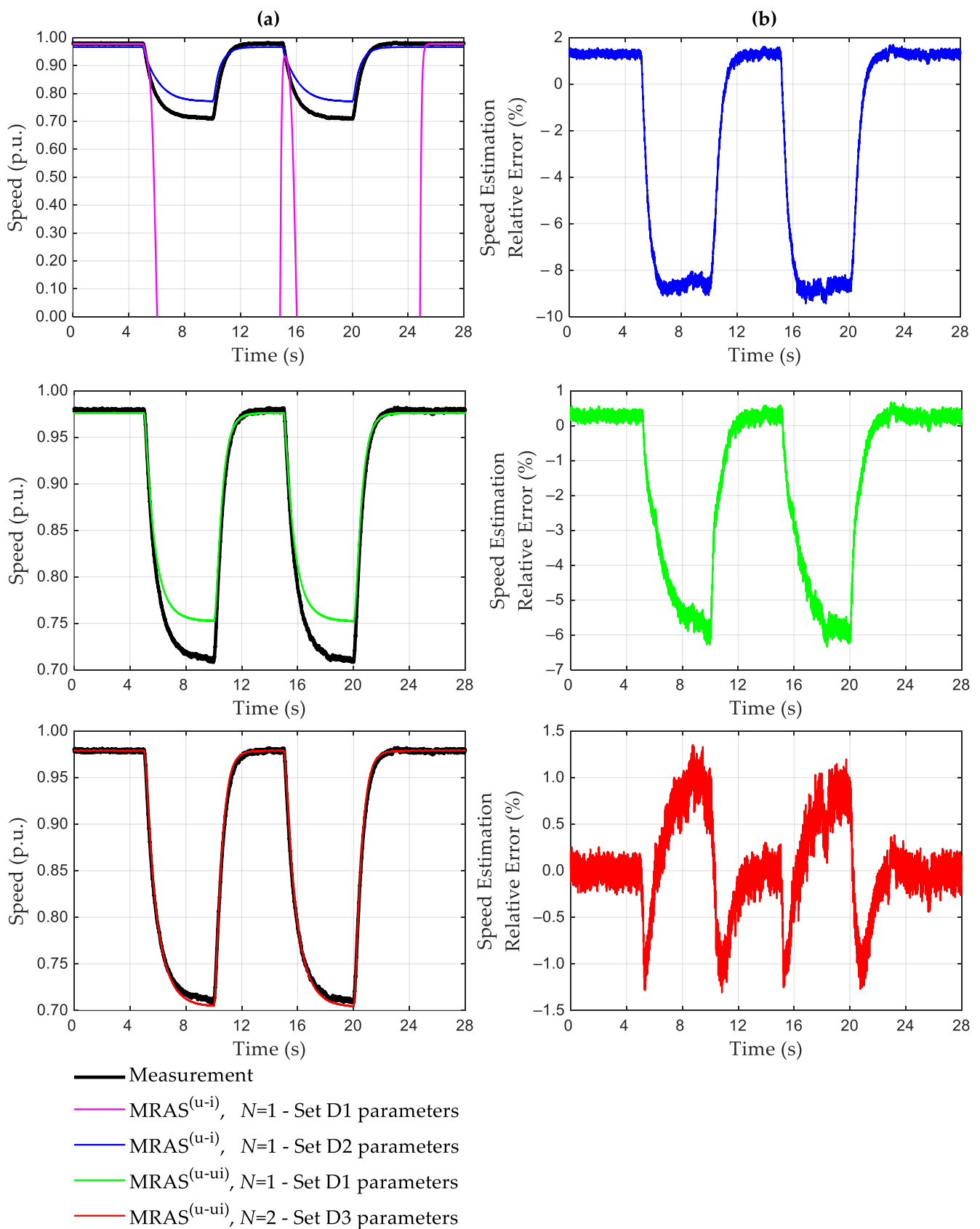
Figure 7. The speed estimation of the tested SR IM: (**a**) the measured and estimated speeds; (**b**) the speed estimation relative errors.

Figure 6a presents the measured speed of the CR IM together with the speed estimates obtained by the tested MRAS-based speed estimators. The relative errors of the speed estimation are shown in Figure 6b. Table 1 lists the maximal and mean relative speed estimation errors. Figure 6 includes the speed estimates obtained by the MRAS$^{(u\text{-}i)}$ and MRAS$^{(u\text{-}ui)}$ when the Set B1 T-type equivalent circuit parameters were applied. The use of this parameter set allowed for a more accurate speed estimation compared to when the Set B2 parameters Set B2 were employed (Table 1).

Table 1. Maximum and mean relative errors (%) of the speed estimation for the tested CR IM.

Speed Estimator	MRAS$^{(u\text{-}i)}$, $N = 1$		MRAS$^{(u\text{-}ui)}$, $N = 1$		MRAS$^{(u\text{-}ui)}$, $N = 2$
Equivalent circuit parameter set	Set B1	Set B2	Set B1	Set B2	Set B3
$\max|\Delta\omega_m^e|$	0.5173	0.7709	0.3481	0.6053	0.3418
$M|\Delta\omega_m^e|$	0.1735	0.1935	0.0793	0.2158	0.0799

All three of the MRAS-based speed estimators that were considered enabled the speed estimation of the CR IM with relative errors not exceeding $\pm 1\%$ in the studied range of slip frequencies (Figure 6 and Table 1). This fact can be associated with the accuracy of the inductance frequency characteristic approximation by the characteristics that resulted from the adopted IM space vector models (Figure 4). In practice, the accuracy was comparable for both IM space vector models, which included either one ($N = 1$) or two ($N = 2$) parallel branches in the rotor equivalent circuit, no matter which parameter set of the T-type equivalent circuit was used in the former (Set B1 or Set B2). However, the slightly better performance of the MRAS$^{(u\text{-}ui)}$ relative to the MRAS$^{(u\text{-}i)}$ was noticeable under the full load (Figure 6).

Figure 7a presents the measured and estimated speed of the SR IM, whilst Figure 7b includes the speed estimation relative errors. The maximal and mean relative errors of the speed estimation for the SR IM are presented in Table 2. In this case, the better performance of the MRAS$^{(u\text{-}i)}$ was achieved with the Set D2 T-type equivalent circuit parameters whereas the MRAS$^{(u\text{-}ui)}$ enabled a more precise speed estimation with the Set D1 parameters (Table 2).

Table 2. Maximum and mean relative errors (%) of the speed estimation for the tested SR IM.

Speed Estimator	MRAS$^{(u\text{-}i)}$, $N = 1$		MRAS$^{(u\text{-}ui)}$, $N = 1$		MRAS$^{(u\text{-}ui)}$, $N = 2$
Equivalent circuit parameter set	Set D1	Set D2	Set D1	Set D2	Set D3
$\max|\Delta\omega_m^e|$	>100	9.4321	6.3380	7.5058	1.3520
$M|\Delta\omega_m^e|$	>100	3.7889	1.9094	3.4092	0.3564

The speed estimates generated by the MRAS$^{(u\text{-}i)}$ and MRAS$^{(u\text{-}ui)}$, developed on the space vector model with the rotor impedance modelled by the single branch of the series equivalent resistance and leakage inductance, were fraught with errors reaching 9.4321% and 6.3380%, 7.5058%, respectively, depending on the parameter set used (Figure 7 and Table 2). Since the PI controllers of the MRAS-based speed estimators guaranteed the fast rate of convergence between the adaptation mechanism functions' components (Figure A4a,b), these errors should be related to the inaccurate approximation of the tested SR IM inductance frequency characteristic in the considered range of slip frequencies (Figure 5). It also should be noted that the MRAS$^{(u\text{-}i)}$ employing the Set D1 parameters did not provide the correct speed estimation when the tested SR IM operated under load. Under these conditions, the speed estimation relative errors exceeded 100% (Figure 7 and Table 2) and

the convergence between the adaptation mechanism functions' components could not be achieved for any gain levels of the MRAS$^{(u-i)}$ PI controller.

The assumed approximation accuracy of the inductance frequency characteristic of the tested SR IM was obtained by the IM space vector model with two parallel connected branches of the series equivalent resistance and leakage inductance. The use of the MRAS$^{(u-ui)}$ devised on such a model translated into a much more precise speed estimation. This configuration of the MRAS$^{(u-ui)}$ enabled a speed estimation with relative errors not exceeding ±1.5% across the whole considered slip frequency range (Figure 7 and Table 2).

5. Conclusions

The investigated MRAS-based speed estimators were tested using open-loop controlled CR and SR IMs operated under the slip frequency changes corresponding to load current changes of up to 1.50 times that of the rated current (Figure A1). The studied slip frequency range was set on purpose to reliably verify the performance of the considered MRAS-based speed estimators under the rotor impedance variability that occurs with the slip frequency changes. These tests indicated the potential industrial applications of the devised speed estimator.

The MRAS-based speed estimators, which were formulated on the IM space vector models with either one ($N = 1$) or two ($N = 2$) parallel connected branches in the rotor equivalent circuit, enabled a comparable speed estimation precision for the tested CR IM. Therefore, there is no need for the design B IMs to employ the speed estimator developed on the IM space vector model where the rotor impedance is modelled by more than one branch of the series rotor equivalent resistance and leakage reactance.

The superiority of the MRAS$^{(u-ui)}$ formulated on the IM space vector model with two ($N = 2$) parallel connected branches in the rotor equivalent circuit became evident for the speed estimation of the SR IM. Such a motor is characterized by significantly greater changes in slip frequency with load current changes compared to the CR IM (Figure A1). Therefore, modelling of the rotor impedance variability by the single branch of the series rotor equivalent resistance and leakage inductance can be insufficient in the case of high-slip IMs. The devised MRAS$^{(u-ui)}$ can be confidently employed in the speed-sensorless state monitoring system for open-loop controlled design D IMs.

Author Contributions: Conceptualization, G.U. and J.R.; methodology, G.U. and J.R.; validation, G.U. and J.R.; investigation, G.U. and J.R.; writing—original draft preparation, G.U.; writing—review and editing, G.U. and J.R.; visualization, G.U.; supervision, J.R. All authors have read and agreed to the published version of the manuscript.

Data Availability Statement: Not applicable.

Appendix A

The rated parameters of the tested CR and SR IMs are listed in Table A1. Tables A2 and A3 present the equivalent circuit parameters of the CR and SR IMs, respectively. Figure A1 presents the current slip characteristics of the tested IMs determined on the data derived under the load curve tests.

**Table A1.** The rated parameters of the tested CR and SR IMs.

Rating	Unit	CR IM	SR IM
Stator voltage	volt (V)	400 (wye)	400 (wye)
Stator frequency	hertz (Hz)	50	50
Stator current	ampere (A)	4.50	2.85
Torque	newton meter (N·m)	15.5	5.9
Rotational speed	revolutions per minute (r/m)	1450	1275

Table A2. The equivalent circuit parameter sets of the tested CR IM. The resistances were corrected to the reference winding temperature of 25 °C.

Equivalent Circuit Parameter Set	$L_{1\sigma}$ (H)	L_m (H)	$R_{2(1)}$ (Ω)	$L_{\sigma2(1)}$ (H)	$R_{2(2)}$ (Ω)	$L_{\sigma2(2)}$ (H)
Set B1	0.0153	0.5000	1.5687	0.0231	–	–
Set B2	0.0147	0.5041	1.6973	0.0219	–	–
Set B3	0.0176	0.4875	2.0812	0.0143	6.9916	0.2146

Table A3. The equivalent circuit parameter sets of the tested SR IM. The individual resistances correspond to the average stator winding temperature of 52 °C registered under the load curve test.

Equivalent Circuit Parameter Set	$L_{1\sigma}$ (H)	L_m (H)	$R_{2(1)}$ (Ω)	$L_{\sigma2(1)}$ (H)	$R_{2(2)}$ (Ω)	$L_{\sigma2(2)}$ (H)
Set D1	0.0847	0.4526	8.3139	0.1106	–	–
Set D2	0.0464	0.5168	16.0648	0.0464	–	–
Set D3	0.0224	0.5018	17.4053	0.0826	19.9513	1.1704
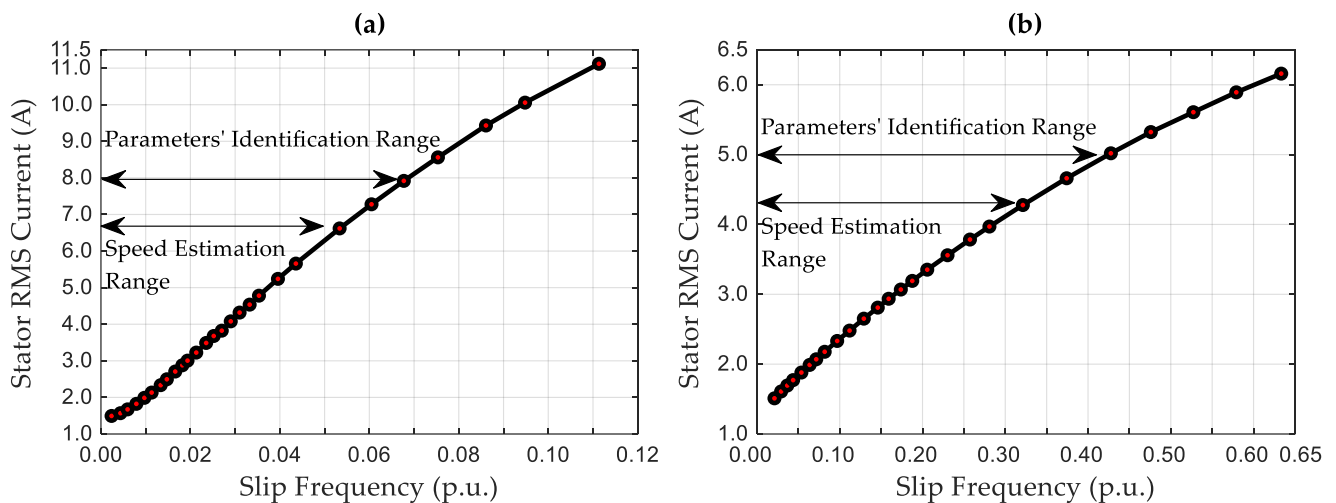
Figure A1. The current slip characteristics of the tested IMs: (**a**) the CR IM; (**b**) the SR IM.

Appendix B

The tested IMs were powered by the programmable AC source AMETEK Model: 3001iX. The programmable electronic load ZSAC4244—H&H GmbH was used to control the armature current of the separately excited DC machine to generate the load torque under the load curve tests and the verification studies of the investigated estimators' performance. The National Instruments USB-6255 high-resolution, multifunction I/O device was employed for data acquisition (DAQ); its configuration and measurement data acquisition were
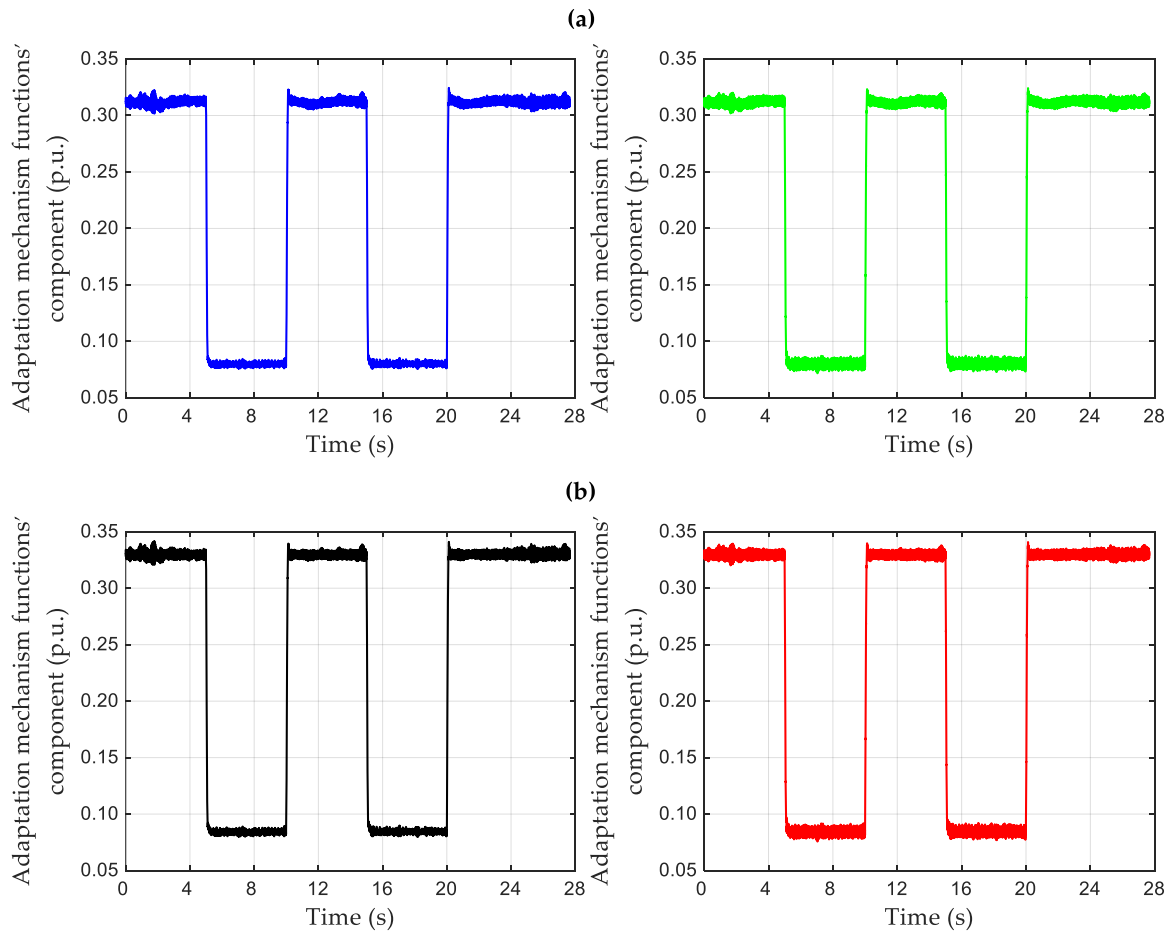
carried out with the use of the National Instruments LabView software. Processing of the measurement data and visualisation of the research results were conducted in the MatLab environment.
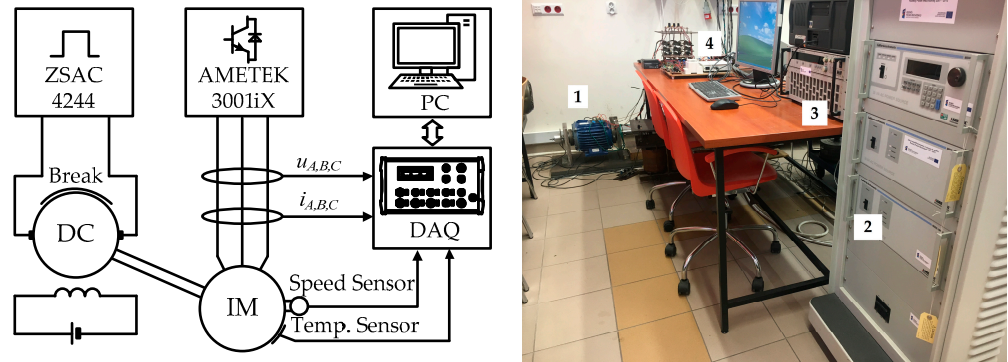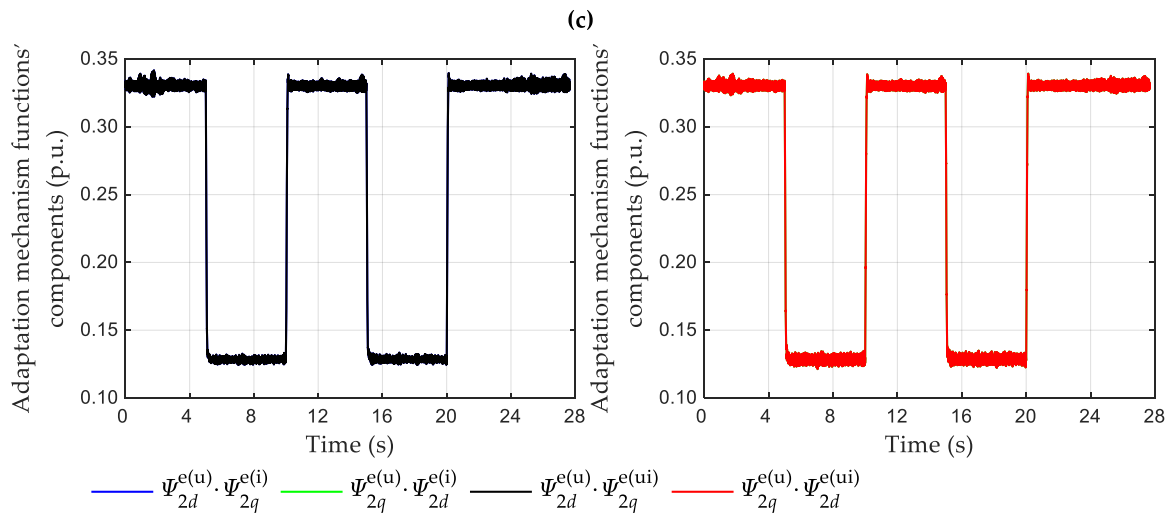

Figure A2. A schematic diagram and picture of the laboratory test bench: 1—tested IM; 2—programmable AC source AMETEK 3001iX; 3—programmable electronic load ZSAC4244; 4—DAQ.

Appendix C

Figures A3 and A4 present the components of the adaptation mechanism functions in the synchronous rotating frame returned by the selected configurations of the MRAS-based speed estimators together with the speed estimates included in the main text of the paper.
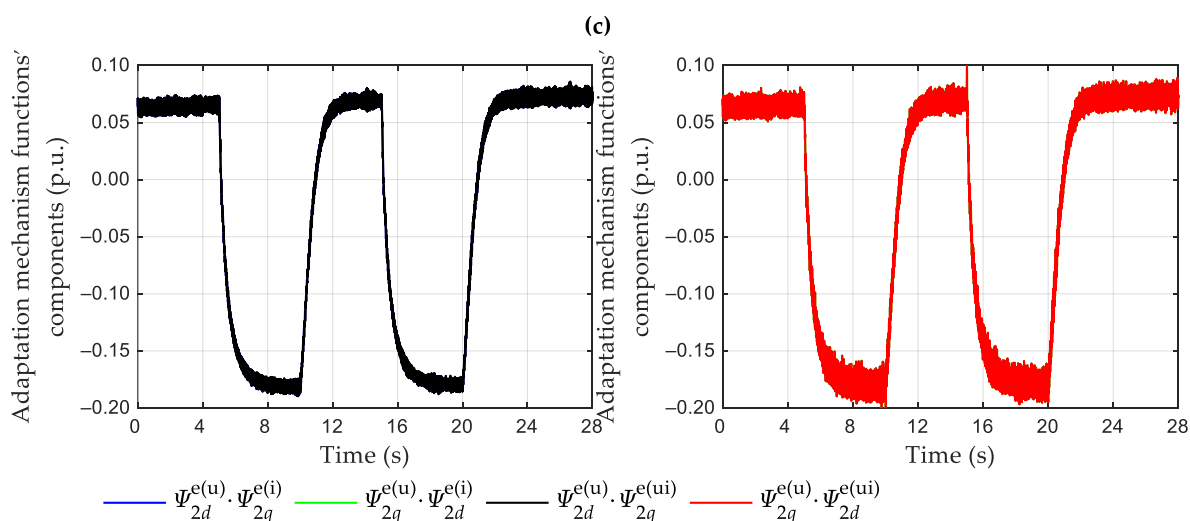
(a)

(b)

Figure A3. *Cont.*

(c)

$$\underline{\hspace{1.5cm}}\ \varPsi_{2d}^{e(u)}\cdot\varPsi_{2q}^{e(i)} \qquad \underline{\hspace{1.5cm}}\ \varPsi_{2q}^{e(u)}\cdot\varPsi_{2d}^{e(i)} \qquad \underline{\hspace{1.5cm}}\ \varPsi_{2d}^{e(u)}\cdot\varPsi_{2q}^{e(ui)} \qquad \underline{\hspace{1.5cm}}\ \varPsi_{2q}^{e(u)}\cdot\varPsi_{2d}^{e(ui)}$$

Figure A3. The components of the adaptation mechanism functions returned by the MRAS[(u-i)] and MRAS[(u-ui)] during the speed estimation of the tested CR IM: (**a**) the MRAS[(u-i)], *N* = 1—set B1 parameters; (**b**) MRAS[(u-ui)], *N* = 1—set B1 parameters; and (**c**) MRAS[(u-ui)], *N* = 2—set B3 parameters.

(a)

(b)

Figure A4. *Cont.*

(c)
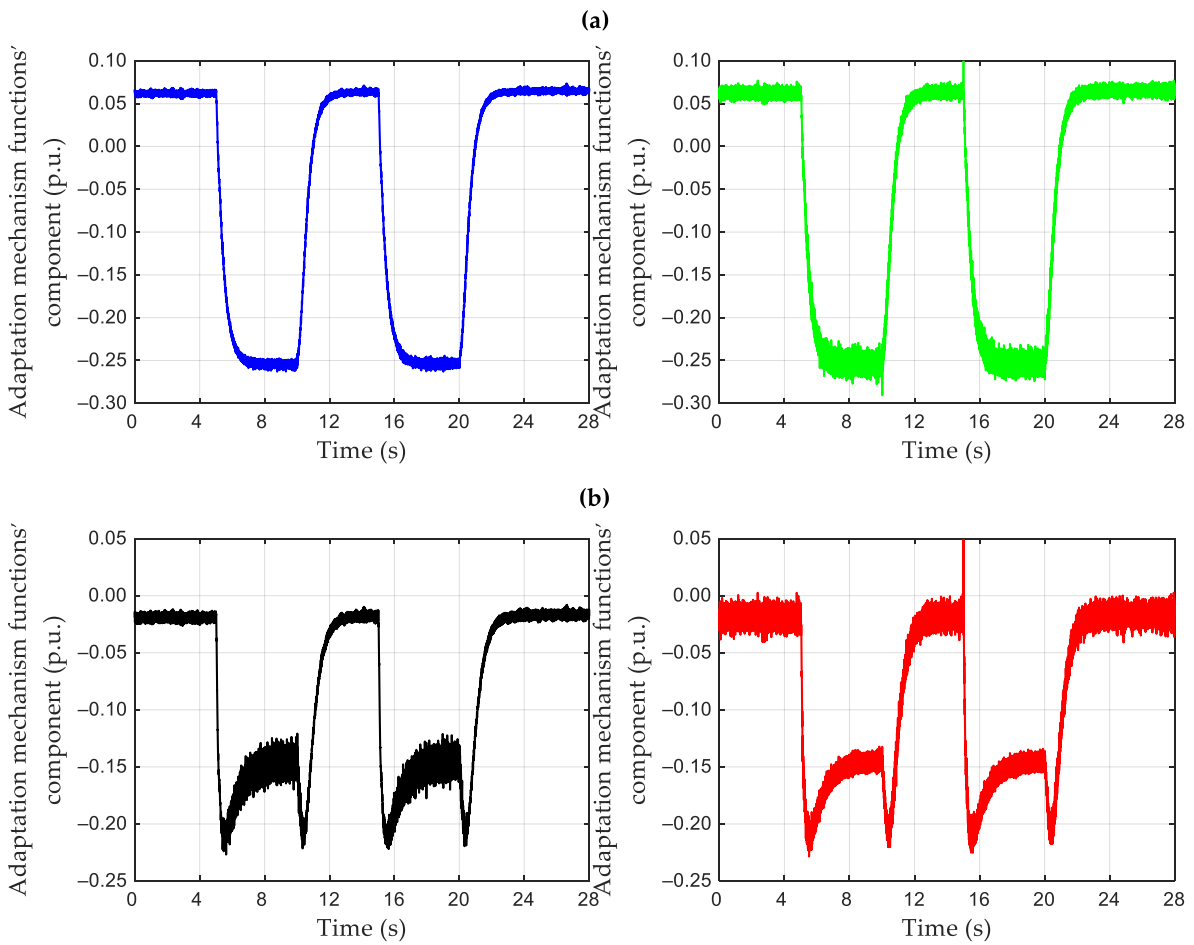
Figure A4. The components of the adaptation mechanism functions returned by the MRAS(u-i) and MRAS(u-ui) during the speed estimation of the tested SR IM: (**a**) the MRAS(u-i), *N* = 1—set D1 parameters; (**b**) MRAS(u-ui), *N* = 1—set D2 parameters; and (**c**) MRAS(u-ui), *N* = 2—set D3 parameters.

References

1. Holtz, J. Sensorless control of induction machines—With or without signal injection? *IEEE Trans. Ind. Electron.* **2008**, *53*, 7–30. [CrossRef]
2. Finch, J.W.; Giaouris, D. Controlled AC Electrical Drives. *IEEE Trans. Ind. Electron.* **2008**, *55*, 481–491. [CrossRef]
3. Xu, D.; Wang, B.; Zhang, G.; Wang, G.; Yu, Y. A review of sensorless control methods for AC motor drives. *CES Trans. Electr. Mach. Syst.* **2018**, *2*, 104–115. [CrossRef]
4. Schauder, C. Adaptive speed identification for vector control of induction motors without rotational transducers. *IEEE Trans. Ind. Appl.* **1992**, *28*, 1054–1061. [CrossRef]
5. Peng, F.-Z.; Fukao, T. Robust speed identification for speed-sensorless vector control of induction motors. *IEEE Trans. Ind. A* **1994**, *30*, 1234–1240. [CrossRef]
6. Teja, A.V.R.; Chakraborty, C.; Maiti, S.; Hori, Y. A New Model Reference Adaptive Controller for Four Quadrant Vector Controlled Induction Motor Drives. *IEEE Trans. Ind. Electron.* **2012**, *59*, 3757–3767. [CrossRef]
7. Zhao, L.; Huang, J.; Liu, H.; Li, B.; Kong, W. Second-Order Sliding-Mode Observer With Online Parameter Identification for Sensorless Induction Motor Drivest. *IEEE Trans. Ind. Electron.* **2014**, *61*, 5280–5289. [CrossRef]
8. Smith, A.N.; Gadoue, S.M.; Finch, J.W. Improved Rotor Flux Estimation at Low Speeds for Torque MRAS-Based Sensorless Induction Motor Drives. *IEEE Trans. Energy Convers.* **2016**, *31*, 270–282. [CrossRef]
9. Pal, A.; Das, S.; Chattopadhyay, A.K. An Improved Rotor Flux Space Vector Based MRAS for Field-Oriented Control of Induction Motor Drives. *IEEE Trans. Power Electron.* **2018**, *33*, 5131–5141. [CrossRef]
10. Kubota, H.; Matsuse, K.; Nakano, T. DSP-based speed adaptive flux observer of induction motor. *IEEE Trans. Ind. Appl.* **1993**, *29*, 344–348. [CrossRef]
11. Harnefors, L.; Hinkkanen, M. Complete stability of reduced-order and full-order observers for sensorless IM drives. *IEEE Trans. Ind. Electron.* **2008**, *55*, 1319–1329. [CrossRef]
12. Chen, B.; Wang, T.; Yao, W.; Lee, K.; Lu, Z. Speed convergence rate-based feedback gains design of adaptive full-order observer in sensorless induction motor drives. *IET Electr. Power Appl.* **2014**, *8*, 13–22. [CrossRef]
13. Vieira, R.P.; Gastaldini, C.C.; Azzolin, R.Z.; Grundling, H.A. Discrete-time sliding mode speed observer for sensorless control of induction motor drives. *IET Electr. Power Appl.* **2012**, *6*, 681–688. [CrossRef]
14. Zaky, M.S.; Metwaly, M.K.; Azazi, H.Z.; Deraz, S.A. A New Adaptive SMO for Speed Estimation of Sensorless Induction Motor Drives at Zero and Very Low Frequencies. *IEEE Trans. Ind. Electron.* **2018**, *65*, 6901–6911. [CrossRef]
15. Lee, K.-B.; Blaabjerg, F. Reduced-order extended luenberger observer based sensorless vector control driven by matrix converter with nonlinearity compensation. *IEEE Trans. Ind. Electron.* **2006**, *53*, 66–75.
16. Kim, Y.-R.; Sul, S.-K.; Park, M.-H. Speed sensorless vector control of induction motor using extended Kalman filter. *IEEE Trans. Ind. Appl.* **1994**, *30*, 1225–1233.
17. Habibullah, M.; Lu, D.D.-C. A Speed-Sensorless FS-PTC of Induction Motors Using Extended Kalman Filters. *IEEE Trans. Ind. Electron.* **2015**, *62*, 6765–6778. [CrossRef]
18. Zerdali, E.; Barut, M. The Comparisons of Optimized Extended Kalman Filters for Speed-Sensorless Control of Induction Motors. *IEEE Trans. Ind. Electron.* **2017**, *64*, 4340–4351. [CrossRef]

19. Zerdali, E. A Comparative Study on Adaptive EKF Observers for State and Parameter Estimation of Induction Motor. *IEEE Trans. Energy Convers.* **2020**, *35*, 1443–1452. [CrossRef]
20. Jayaramu, M.L.; Suresh, H.N.; Bhaskar, M.S.; Almakhles, D.; Padmanaban, S.; Subramaniam, U. Real-Time Implementation of Extended Kalman Filter Observer with Improved Speed Estimation for Sensorless Control. *IEEE Access* **2021**, *9*, 50452–50465. [CrossRef]
21. Akatsu, K.; Kawamura, A. Sensorless very low-speed and zero-speed estimations with online rotor resistance estimation of induction motor without signal injection. *IEEE Trans. Ind. Appl.* **2000**, *36*, 764–771. [CrossRef]
22. Ohyama, K.; Asher, G.M.; Sumner, M. Comparative analysis of experimental performance and stability of sensorless induction motor drives. *IEEE Trans. Ind. Electron.* **2006**, *53*, 178–186. [CrossRef]
23. Vaclavek, P.; Blaha, P.; Herman, I. AC Drive Observability Analysis. *IEEE Trans. Ind. Electron.* **2013**, *60*, 3047–3059. [CrossRef]
24. Harnefors, L.; Hinkkanen, M. Stabilization Methods for Sensorless Induction Motor Drives—A Survey. *IEEE J. Emerg. Sel. Top. Power Electron.* **2014**, *2*, 132–142. [CrossRef]
25. Chen, J.; Huang, J. Stable Simultaneous Stator and Rotor Resistances Identification for Speed Sensorless IM Drives: Review and New Results. *IEEE Trans. Power Electron.* **2018**, *33*, 8695–8709. [CrossRef]
26. Aiello, M.; Cataliotti, A.; Nuccio, S. An induction motor speed measurement method based on current harmonic analysis with the chirp-Z transform. *IEEE Trans. Instrum. Meas.* **2005**, *54*, 1811–1819. [CrossRef]
27. Zhao, L.; Huang, J.; Chen, J.; Ye, M. A Parallel Speed and Rotor Time Constant Identification Scheme for Indirect Field Oriented Induction Motor Drives. *IEEE Trans. Power Electron.* **2016**, *31*, 6494–6503. [CrossRef]
28. Song, X.; Wang, Z.; Li, S.; Hu, J. Sensorless Speed Estimation of an Inverter-Fed Induction Motor Using the Supply-Side Current. *IEEE Trans. Energy Conv.* **2019**, *34*, 1432–1441. [CrossRef]
29. Degnert, M.W.; Lorend, R.D. Using multiple saliencies for the estimation of flux, position, and velocity in AC machines. *IEEE Trans. Ind. Appl.* **1998**, *34*, 1097–1104. [CrossRef]
30. Caruana, C.; Asher, G.M.; Sumner, M. Performance of HF signal injection techniques for zero-low-frequency vector control of induction Machines under sensorless conditions. *IEEE Trans. Ind. Electron.* **2006**, *53*, 225–238. [CrossRef]
31. Staines, C.S.; Asher, G.M.; Sumner, M. Rotor-position estimation for induction machines at zero and low frequency utilizing zero-sequence currents. *IEEE Trans. Ind. Appl.* **2006**, *42*, 105–112. [CrossRef]
32. Garcia, P.; Briz, F.; Raca, D.; Lorenz, R.D. Saliency-Tracking-Based Sensorless Control of AC Machines Using Structured Neural Networks. *IEEE Trans. Ind. Appl.* **2007**, *43*, 77–86. [CrossRef]
33. Yoon, Y.-D.; Sul, S.-K. Sensorless Control for Induction Machines Based on Square-Wave Voltage Injection. *IEEE Trans. Power Electron.* **2014**, *29*, 3637–3645. [CrossRef]
34. Wang, K.; Chen, B.; Shen, G.; Yao, W.; Lee, K.; Lu, Z. Online Updating of Rotor Time Constant Based on Combined Voltage and Current Mode Flux Observer for Speed-Sensorless AC Drives. *IEEE Trans. Ind. Electron.* **2014**, *61*, 4583–4593. [CrossRef]
35. Marcetic, D.P.; Vukosavic, S.N. Speed-Sensorless AC Drives with the Rotor Time Constant Parameter Update. *IEEE Trans. Ind. Electron.* **2007**, *54*, 2618–2625. [CrossRef]
36. Levy, W.; Landy, C.H.; McCulloch, M.D. Improved models for the simulation of deep bar induction motors. *IEEE Trans. Energy Convers* **1990**, *2*, 393–400. [CrossRef]
37. Healey, R.C.; Williamson, S.; Smith, A.C. Improved cage rotor models for vector controlled induction motors. *IEEE Trans. Ind. Appl.* **1995**, *4*, 812–822. [CrossRef]
38. Rolek, J.; Utrata, G. An identification procedure of electromagnetic parameters for an induction motor equivalent circuit including rotor deep bar effect. *Arch. Electr. Eng.* **2018**, *2*, 279–291.
39. Mölsä, E.; Saarakkala, S.E.; Hinkkanen, M.; Arkkio, A.; Routimo, M. A Dynamic Model for Saturated Induction Machines with Closed Rotor Slots and Deep Bars. *IEEE Trans. Energy Convers* **2020**, *35*, 157–165. [CrossRef]
40. Seok, J.-K.; Sul, S.-K. Pseudorotor-flux-oriented control of an induction machine for deep-bar-effect compensation. *IEEE Trans. Ind. Appl.* **1998**, *34*, 429–434. [CrossRef]
41. Utrata, G.; Rolek, J.; Kaplon, A. The Novel Rotor Flux Estimation Scheme Based on the Induction Motor Mathematical Model Including Rotor Deep-Bar Effect. *Energies* **2019**, *12*, 2676. [CrossRef]
42. Landau, I.D. *Adaptive Control: The Model Reference Approach*; Marcel Dekker: New York, NY, USA, 1979.
43. *PN-EN 60034-28*; 2013 Rotating Electrical Machines—Part 28: Test Methods for Determining Quantities of Equivalent Circuit Diagrams for Three-Phase Low Voltage Cage Induction Motors. Polski Komitet Normalizacyjny: Warszawa, Poland, 2013.
44. *IEEE Std 112-2017 (Revision of IEEE Std 112-2004)*; Standard Test Procedure for Polyphase Induction Motors and Generators . IEEE Power Engineering Society: New York, NY, USA, 2004. [CrossRef]